Ultrastrong coupling regime of light-matter interaction

by

Miquel Àngel Pérez Puigdomènech

Under the Guidance of

Alba Torras-Coloma and Dr. Pol Forn-Díaz

IFAE
Institut de Física d'Altes Energies

Academic tutor

Prof. Dr. Verònica Ahufinger

UAB
Universitat Autònoma de Barcelona

Physics BSc. Undergraduate Thesis

UNIVERSITAT AUTÒNOMA DE BARCELONA

January 19, 2024

Convocatòria Febrer 2024

DECLARACIÓ D'AUTORIA DEL TREBALL DE GRAU

Jo, Miquel Àngel Pérez, amb DNI 48173181A, i estudiant del Grau en Física de la Universitat Autònoma de Barcelona, en relació amb la memòria del treball de final de Grau presentada per a la seva defensa i avaluació durant la convocatòria de febrer del curs 2023-2024, declara que:

- El document presentat és original i ha estat realitzat per la seva persona.
- El treball s'ha dut a terme principalment amb l'objectiu d'avaluar l'assignatura de treball de grau en física en la UAB, i no s'ha presentat prèviament per ser qualificat en l'avaluació de cap altra assignatura ni aquesta ni en cap altra universitat.
- En el cas de continguts de treballs publicat per terceres persones, l'autoria està clarament atribuïda, citant les fonts degudament.
- En els casos en els quals el meu treball s'ha realitzat en col·laboració amb altres investigadors i/o estudiants, es declara amb exactitud quines contribucions es deriven del treball de tercers i quines es deriven de la meva contribució.
- A l'excepció dels punts esmentat anteriorment, el treball presentat és de la meva autoria.

Signat:

MIQUEL ANGEL PEREZ PUIGDOMÉNECH - DNI 48173181A

Digitally signed by MIQUEL ANGEL PEREZ PUIGDOMÉNECH - DNI 48173181A
Date: 2024.01.19 10:41:46 +01'00'

DECLARACIÓ D'EXTENSIÓ DEL TREBALL DE GRAU

Jo, Miquel Àngel Pérez Puigdomènech, amb DNI 48173181A, i estudiant del Grau en Física de la Universitat Autònoma de Barcelona, en relació amb la memòria del treball de final de Grau presentada per a la seva defensa i avaluació durant la convocatòria de Febrer del curs 2023-2024, declara que:

- El nombre total de paraules incloses en les seccions des de la introducció a les conclusions és de 7376 paraules.
- El nombre total de figures és de 13.

En total el document, comptabilitza:

$$7376 \text{ paraules} + 13 \text{ x } 200 \text{ paraules/figura} = 9976 \text{ paraules}$$

Que compleix amb la normativa al ser inferior a 10000.

Signat:

MIQUEL ANGEL PEREZ PUIGDOMÉNECH - DNI 48173181A

Digitally signed by MIQUEL ANGEL PEREZ PUIGDOMÉNECH - DNI 48173181A
Date: 2024.01.19 10:42:15 +01'00'

Abstract

In this thesis we have studied from a numerical point of view the system consisting of a flux qubit galvanically coupled to an LC oscillator in the ultrastrong coupling regime. We demonstrate for the 3 Josephson Junction with inductance flux qubit that this regime can be achieveble with the designed parameters. Parallely, it is also demonstrated that this regime can be obtained experimentally with aluminum thin wires, and its calibration is performed.

Contents

Chapter 1

Introduction and Objectives

1.1 Introduction

This thesis aims to explore the ultrastrong coupling regime (USC) of light-matter interaction, using galvanic contacts in tandem with superconducting quantum bits. These are obtained with superconducting quantum circuits, which, with only simple building blocks, allow the design of chips with different properties and purposes.

The number of applications is unfathomable in the broader field of superconducting quantum qubits. For instance, in the past few years, the interest in this technology has grown and companies such as Google [1], IBM [2], or many others have used it to build quantum computers. However, superconducting quantum circuits (SQCs) are not only useful for building quantum computers. The integration of superconducting qubits has opened doors to new frontiers of exploration in quantum computing [3], quantum communication [4], and quantum simulation [5]. These qubits serve as the building blocks for innovative technologies, driving progress in fields as diverse as optimization problems, cryptography, and material science simulations.

As previously mentioned, we are interested in studying the USC because the applications of this platform are many. In recent years, the study of light-matter interaction in these types of systems has been on the rise. One of the reasons for this is that SQCs systems are very customizable and allow studying phenomena that are not accessible or observable in typical systems (such as atoms with cavities). Since the first time that the ultrastrong coupling regime was obtained with SQCs [6], the range of potential applications proven by USC extends extensively, encompassing areas such as quantum information processing [7], quantum metrology [8], nonlinear optics [9], quantum optomechanics [10], quantum plasmonics [11] and even branches like chemistry, quantum electrodynamics and materials science [12].

1.2 Objectives

This study aims to understand the basics of superconducting quantum circuit technology and put special interest in the study of light-matter interactions in this platform. With this aim, it will be important to gain a comprehensive understanding of the Quantum Rabi model, which will enable the exploration of the USC using galvanic couplings in superconducting qubits.

The mathematical characterization of our system is a pivotal aspect of this study. We aim to study the quantization of the system, the Hamiltonian derivation, a numerical study of eigenvectors and eigenvalues and the ability to calculate the coupling coefficient in the ultrastrong coupling regime for a flux qubit galvanically coupled to a resonator.

On a parallel track, an initial experimental characterization of the device will be carried out. This will involve the study of the kinetic inductance of thin aluminum wires, since it is an important parameter to calibrate the coupling of the system in the final device.

Chapter 2

Theoretical background

In this section, we will introduce superconducting quantum circuits, the main circuit elements and one key element for the experiments that will be shown below: the flux qubit. Following this, we will explain the concept of the Quantum Rabi model and how superconducting quantum circuits can help us study regimes of interaction beyond the strong coupling regime, a regime often unattainable in other fields in Quantum Optics.

2.1 Superconducting Quantum Circuits

A superconducting circuit can be envisioned as an integrated circuit crafted from superconducting materials. The introduction of superconductivity dramatically transforms the circuit's behavior, as classical variables evolve into quantum operators. Consequently, the current I in a circuit is no longer a simple scalar but is expressed as an operator $\hat{I}$ that can act on the circuit's wavefunction ($|\Phi\rangle$). This allows, for instance, a superposition of two current states flowing in opposite directions to occur within a quantum circuit [13].

A central element is the so-called Josephson Junction, a special connection between two superconductors connected by an insulator barrier that facilitates the flow of supercurrent. Here, Cooper pairs, which are pairs of electrons in a superconductor, tunnel through the junction, allowing for the manifestation of quantum phenomena. These junctions constitute the main building block of superconducting qubits[1]. Often referred to as artificial atoms, these circuits provide the remarkable ability to finely adjust their parameters within ranges that are challenging, if not impossible, with natural atoms [15].

[1]These fundamental units of quantum information are made with SQCs thanks to their characteristics of low dissipation, low susceptibility to noise, and nonlinearity [14].

2.1.1 Circuit elements

The behavior of quantum circuits is quite similar to classical circuits. Both involve a set of dynamic equations that describe the evolution of circuit parameters, whether they are voltage-related or current-related. This information can also be expressed using a Hamiltonian, a mathematical framework commonly used in quantum mechanics. However, a distinctive feature emerges in quantum circuits: the circuit variables are represented by quantum operators, and their interactions adhere to commutation relations [16].

One can think of any electrical circuit as a network of branches made up of two-terminal components like capacitors and inductors. Each component is examined under the lumped-element approximation [17] when dealing with SQCs. This approximation is valid when the size of the component is significantly smaller than the wavelength of the frequencies involved. This condition is satisfied for microwave frequencies, which are on the order of centimetres, whereas the circuit elements are on the order of micrometres [18].

In the next subsections, we examine the different circuit elements that will be used throughout the thesis [19].

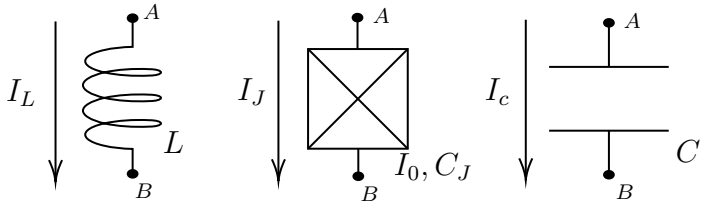

FIGURE 2.1: Diagram of different circuit elements that a superconducting quantum circuit may have. From left to right: an inductor, a Josephson junction and a capacitor.

2.1.1.1 Josephson Junctions

A Josephson Junction (JJ) is a component in an electrical circuit (depicted at the centre in Figure 2.1) consisting of a tunnel junction between two superconductors. This junction exhibits a remarkable quantum phenomenon known as the Josephson effect. The Josephson effect refers to the ability of Cooper pairs in a superconductor to tunnel through the insulating barrier, allowing for a coherent coupling between the superconductors [20]. Its properties are defined by its capacitance, denoted as C_J, and the Josephson energy $E_J = \frac{\Phi_0}{2\pi} I_0$, where $\Phi_0 = \frac{h}{2e}$ is the superconducting flux quantum, being e the electron charge, h the Planck's constant and I_0 the critical current of the junction. The current of a JJ is

$$I_J = I_0 \sin\left(\frac{2\pi}{\Phi_0}(\phi_b - \phi_a)\right), \tag{2.1}$$

expressed in terms of the magnetic flux ϕ and since the relationship between the current and voltage across the junction is nonlinear, Josephson junctions are a crucial element for qubits[2]. Typical values range in the $I_0 \sim 10 - 500$ nA, leading to $E_J/h \sim 5 - 250$ GHz [21].

2.1.1.2 Inductor

An inductance is a component (see first panel of Figure 2.1) that induces a voltage when a change in the current passes through it. Its behaviour is defined by a property known as inductance L, creating a resulting current

$$I_L = \frac{\phi_b - \phi_a}{L}, \tag{2.2}$$

which is linear to the flux difference. Typical values of L in SQCs range in the pH in micron-sized loops to nH when using superinductors [22]. The ratio between the Josephson inductance and the Junction Energy is defined as $\beta_L \equiv \frac{2\pi}{\Phi_0} L I_0$.

2.1.1.3 Capacitor

A capacitance is a circuit element (see first panel of Figure 2.1) that stores charge and creates a current

$$I_C = C(\ddot{\phi}_b - \ddot{\phi}_a), \tag{2.3}$$

which is characterized by its capacitance C and its charging energy $E_c = \frac{e^2}{2C}$ corresponds to the energy transferred by an electron. Typical values of C range in the fF to pF, with E_C taking values in the MHz to GHz range [23]. The value of C will usually be defined by the geometry of the circuit.

[2]The non-linearity of Josephson junctions give rise to anharmonicity, an important feature when a qubit is targeted, since the two levels have a distinguishable energy transition from the other levels

2.2 Circuit quantization

In this section, we will delve into the principles of circuit quantization, exploring the transformation from classical to quantum description.

The process of deriving a quantized Hamiltonian from an electrical circuit governed by quantum mechanical principles involves a systematic approach that is described in [16] and we provide a summary of the main steps needed to quantize a superconducting circuit. This quantization will only hold at temperatures below $\hbar\omega/k_B$ where k_B is the Boltzmann constant and $\hbar\omega$ characteristic energy scale of excitations. We also require excitations well below the superconducting gap [24].

Commencing with Kirchhoff's laws, the procedure establishes equations of motion for the system's degrees of freedom, leading to the formulation of the Lagrangian. Subsequently, the Hamiltonian is derived and ultimately subjected to quantization.

Firstly, we need to identify all the nodes in the circuit and designate one as the ground reference point. Starting from this ground node, establish connections to all other nodes by following a single path. The branches chosen in this process constitute the spanning tree. The remaining branches are known as closure branches, and their associated flux is determined by the circuit constraints.

To maintain consistency, we arbitrarily assign a direction for the current flow in each branch; the specific direction chosen does not affect the analysis, but it is necessary for coherence. For spanning branches, the relationship between node and branch flux is $\phi = \phi_j - \phi_i$.

However, for closure branches, a flux may be present. If closure branches enclose a closed loop bordered by inductances or Josephson junctions, an additional flux term is included in the relationship. The sign of this flux is not explicitly defined, but consistency is crucial. In this context, choose a direction for the flux (either escaping from the page or going inwards) and add it to the relationship when the direction of the branch's current coincides with that induced by the flux. Subtract it if they go in opposite directions. Consequently, when there's a flux, the relation becomes

$$\phi = \phi_j - \phi_i \pm \phi_{ext}. \tag{2.4}$$

When every flux of the system is well-defined, Kirchoff's current conservation equation for each node are used, ensuring that the sum of all currents at the node equals zero. The following step is to integrate all equations of motion to obtain the Lagrangian, knowing that

$$\frac{\mathrm{d}}{\mathrm{d}t}\left(\frac{\partial \mathcal{L}}{\partial \dot{\phi}_i}\right) = \frac{\partial \mathcal{L}}{\partial \phi_i}. \tag{2.5}$$

Defining the node charges as the canonically conjugate momenta of the node fluxes

$$q_i = \frac{\partial \mathcal{L}}{\partial \dot{\phi}_i}. \tag{2.6}$$

Then, the Hamiltonian can be found by using the Legendre transformation [25],

$$\mathcal{H} = \sum_i q_i \dot{\phi}_i - \mathcal{L}. \tag{2.7}$$

To quantize the Hamiltonian one just has to promote the flux and the charge to quantum mechanical operators

$$\begin{cases} \phi_i \longrightarrow \hat{\phi}_i \\ q_i \longrightarrow \hat{q}_i \end{cases} \tag{2.8}$$

that must obey the commutation relations

$$\left[\hat{\phi}_i, \hat{q}_j\right] = i\hbar\delta_{ij}. \tag{2.9}$$

where δ_{ij} is Kronecker's delta. Using flux and charge operators as quantum mechanical operators, the Hamiltonian $\hat{\mathcal{H}}$ associated with the studied system will be obtained. This Hamiltonian will enable us to derive the circuit's wavefunction by solving the Schrödinger equation.

2.3 Flux qubits

In the context of this thesis, a flux qubit galvanically coupled to a resonator will be studied. The choice of qubit is motivated by two main points: firstly, flux qubits are the main technology developed in the IFAE QCT group. Secondly, there is an interest in using an inductive-type coupling, thus the best approach is to use a flux-type qubit.

Flux qubits are engineered to possess, as qubit states, two eigenstates originating from the inductive component of the Hamiltonian. As a consequence, the typical outcome involves associating states $|0\rangle$ and $|1\rangle$ with two supercurrent states circulating without dissipation along a superconducting loop. To induce these supercurrents, the enclosed flux in the loop is adjusted, leading to frustration and resulting in either two distinct or degenerate configurations of branch fluxes. This condition often corresponds to the presence of permanent currents circulating on the loop [26].

If an external magnetic flux is threaded through this loop with magnitude $\phi_{ext}/\Phi_0 = f = 0.50$, the two lowest energy quantum states are approximately the symmetric and antisymmetric superposition of counter-circulating persistent-current states, arising a two-level system state that will perform as a qubit. The most commonly used in research are the RF-SQUID and the three-junction flux qubit. Even though these two will be studied as candidates for USC in Chapter 3, in this section we provide their main features.

2.3.1 RF-SQUID

In literature, often referred to as Radio Frequency Superconducting Qubit Interference Device (RF-SQUID). The RF-SQUID typically consists of a superconducting loop with inductance interrupted by one Josephson junction. These junctions, formed by thin insulating barriers between superconducting electrodes, allow quantum tunnelling of Cooper pairs.

However, its size can pose challenges as the qubit's sensitivity to stray magnetic fields increases, its lifespan diminishes under conditions analogous to other qubits [23], and it requires an inductor, which is an important drawback.

2.3.2 Three-junction flux qubit

The contemporary design of a flux qubit, employing three junctions, represents a more recent development compared to the traditional understanding of a flux qubit [27]. By introducing a magnetic flux through the loop, we induce frustration, resulting in a degenerate ground state. The degeneracy of this ground state is solely resolved by quantum fluctuations. An advantageous aspect of this design is that the multiwell structure is exclusively formed through Josephson junctions, eliminating the need for additional inductors. Consequently, this design may be significantly more compact, potentially on the scale of a few micrometres.

Some advantages of Three-Junction Flux Qubit vs. RF-SQUID [28]:

1. **Simplified Construction:** Elimination of the need for additional inductors simplifies the construction process, potentially reducing fabrication complexity and costs.

2. **Reduced Sensitivity to Stray Magnetic Fields:** The three-junction flux qubit may exhibit lower sensitivity to stray magnetic fields, contributing to improved stability in various environments.

3. **Potential for Quantum Information Processing:** With advantages in size and construction, the three-junction flux qubit, like the RF-SQUID, holds potential for applications in quantum information processing.

These reasons will make the three junction flux qubit, in the end, a better candidate beforehand.

2.4 Quantum Rabi Model

In the last sections, we have introduced the basics of superconducting quantum circuits. Now we will introduce the quantum model needed to understand light-matter interaction in these systems. The Quantum Rabi Model [29] is a quantum model employed to describe the interaction between a two-level system and a resonator. In this thesis, a flux qubit creates an artificial two-level system, which is galvanically coupled with a resonator. This system effectively creates a ground state $|0\rangle$ and an excited state $|1\rangle$, isolated because of anharmonicity. The interaction with the quantized electromagnetic field mode is encapsulated in the Hamiltonian, with key parameters being the qubit frequency ω_{01}, representing the energy difference between the qubit states, and the resonator frequency ω_r, characterizing the energy states of the microwave field. The Rabi frequency g stands out as the parameter that describes the strength of coupling between light and matter. The Hamiltonian takes the following form

$$\hat{\mathcal{H}} = \frac{\hbar\omega_{01}}{2}\hat{\sigma}_z + \hbar\omega_r\hat{a}^\dagger\hat{a} + \hbar g\hat{\sigma}_x(\hat{a} + \hat{a}^\dagger). \tag{2.10}$$

Here, $\hat{\sigma}_z$ and $\hat{\sigma}_x$ denote the Pauli matrices representing the qubit operators, and $\hat{a}$ and $\hat{a}^\dagger$ are the annihilation and creation operators for photons, respectively. We can identify the different terms of the Hamiltonian

$$\hat{\mathcal{H}} = \hat{\mathcal{H}}_{qubit} + \hat{\mathcal{H}}_{res} + \hat{\mathcal{H}}_{int}, \tag{2.11}$$

corresponding with the one of the qubit, the resonator, and the interaction, respectively.

When the coupling is weak ($g/\omega_r \ll 1$), which is common in the Quantum Optics field, the Rotating Wave Approximation (RWA) is an approximation that simplifies the interaction term by neglecting fast-oscillating terms. Often, this model is referred to as the Jaynes-Cummings Model and yields the following Hamiltonian

$$\hat{\mathcal{H}}_{JC} = \frac{\hbar\omega_{01}}{2}\hat{\sigma}_z + \hbar\omega_r\hat{a}^\dagger\hat{a} + \hbar g(\hat{\sigma}_+\hat{a} + \hat{\sigma}_-\hat{a}^\dagger), \tag{2.12}$$

being $\hat{\sigma}_+$ and $\hat{\sigma}_-$ the raising and lowering operators for the qubit. The RWA assumption is justified when the the qubit and field frequencies are near resonance ($\omega_{01} - \omega_r \ll \omega_{01} + \omega_r$) and the interaction is weak [30].

The RWA significantly simplifies the mathematical treatment of the Rabi model. However, in some cases as in this thesis, the neglected counter-rotating terms may become relevant, especially in situations involving strong qubit-field coupling or when considering more complex quantum systems.

2.5 Ultrastrong Coupling Regime

Up to this part of the thesis, we have described the system as a qubit and a quantum resonator that interact. Nevertheless, as the coupling between these systems intensifies, the Jaynes-Cummings Model (2.12) is not correct. That is because the qubit and the resonator start to hybridize as the coupling increases. In such cases, it becomes impractical to analyze them independently, leading to their classification as the Ultrastrong Coupling Regime where $0.1 \lesssim g/\omega_r$ [21].

Since the first SQCs that achieved the USC regime [6], these have been widely used since they can be designed or even tuned *in situ* [12]. Some strategies to couple a circuit qubit that can be done are geometrical inductances, capacitive coupling, Josephson inductance... However, this thesis has targeted the use of kinetic inductances, because of their promising high inductance, as the source of coupling, shared by the resonator and the qubit. Since these inductances are obtained with narrower wires, this method can achieve the USC regime while controlling the size of the chip [21]. To understand the physics behind kinetic inductors and superinductor materials in superconducting circuits, the next brief section is presented.

2.6 Kinetic inductance and superinductor materials

In superconducting materials, Cooper pairs can move freely for a long distance without scattering. This makes the kinetic inductance of a superconductor non-negligible. One candidate to present a high kinetic inductance is disordered superconductors. Since these superconductors possess grains of oxides or nitrides, they can act as a sum of small Josephson junctions, creating an effective inductance below the superconducting critical temperature. Another possibility is narrowing thin aluminum wires, which force Cooper pairs to collide. A first approximation can be made to predict this kinetic inductance [31]

$$L_{kin,\square} = \frac{0.18\hbar}{k_B}\frac{R_{n,\square}}{T_c}, \tag{2.13}$$

where $R_{n,\square}$ is the normal state sheet resistance[3] of the material at 4K and $T_c = 1.32\pm0.02$ K [32] is the critical temperature of aluminium for 20 mm thickness. Since this equation depends proportionally on its resistance, we will target fabricated chips that have long and narrow wires, achieving the largest resistance possible. Some notable candidates as superinductors are granular aluminum (GrAl) [32] or aluminium nitride (NitrAl) [33]. Nonetheless, thin aluminum wires are easier to fabricate since do not require evaporation with gases and can achieve large inductances as well. These will later be studied in Section 4.5.

[3] In the field of SQCs, since we work with materials with small thickness compared with its size, it is convenient to express variables in terms of a square ($\square$), defined as the surface of a square with sizes equals to the width of the thin wire studied.

Chapter 3

Numerical and experimental methods

In this Section, we present the two numerical methods applied in the thesis to solve the Hamiltonian associated with the different systems studied, as well as the experimental setup to measure the resistance of thin aluminum wires done at IFAE QCT lab.

3.1 Numerical approach: Finite dimension diagonalization

Once a Hamiltonian of the system is derived, our final task is to obtain its spectra and the eigenstates of the system. A numerical approach must be taken, since its Hamiltonian possesses non-linear terms and an analytical solution does not exist, or is not known. In this thesis, two methods have been used. For simpler systems (those containing 2-3 variables) the diagonalization can be done by calculating each matrix element on a given basis. Nevertheless, since more complex systems can have higher computational complexity, libraries optimized for these calculations are used nowadays for researchers, such as *CircuitQ* [34] or *SCQubits* [35].

3.1.1 Matrix element calculations

In this section, we will introduce two distinct mathematical representations for these operators, each associated with its own set of states in their respective Hilbert spaces. It is important to note that defining representations of these operators becomes necessary for calculating the system's wavefunction and eigenenergies.

Charge and flux, within the realm of quantum mechanics, differ from momentum and position operators commonly encountered in classical mechanics. Charge, denoted as $\hat{q}$, is a discrete operator proportional to the number of Cooper pairs: $\hat{q} = -2e\hat{n}$. On the other hand, the flux operator, $\hat{\phi}$, is linked to the superconducting

phase ϕ, expressed as $\hat{\phi} = 2\pi\hat{\Phi}/\Phi_0$. Consequently, the flux operator exhibits a periodic representation. This characteristic implies that plane waves are not suitable representations for these operators, necessitating the introduction of a new phase-number representation.

- In the phase representation, the circuit wavefunction

$$|\Psi\rangle = \int_0^{2\pi} d\phi_1 ... \int_0^{2\pi} d\phi_N \, |\Psi(\phi_1, ..., \phi_N)|\phi_1, ..., \phi_N\rangle \tag{3.1}$$

  expands over states with a well-defined value of the node phase $|\phi_i\rangle$. For instance, one basis which will be convenient to use is the harmonic eigenbasis

$$|k\rangle = \left(\frac{m\omega}{2^{2k}\pi\hbar k!}\right)^{1/4} H_k\left(\sqrt{\frac{m\omega}{\hbar}}\phi\right) e^{-\frac{m\omega\phi^2}{2\hbar}} \tag{3.2}$$

  where H_k is the k_{th} Hermite function [36], m is the mass and ω is the frequency of the oscillator.

- The number representation will depict the states with a given number of excess Cooper pairs $|n\rangle$, utilizing the fact that the charge operator is defined as the sum of projectors onto a well-defined number of Cooper pairs,

Since finding the exact solution of the qubit's Hamiltonian would require the calculation of an infinite-sized matrix, a truncation of the matrix element basis is needed [16]. To carry out this step, the convergence of the solution will have to be checked. Depending on the form of each Hamiltonian studied, one of the two representations will be used, targeting the smallest base possible. For instance, in qubit applications, the energy of the Josephson Junction is usually bigger than the energy of the Cooper pairs, implying that a state with many Cooper pairs is highly improbable, allowing a base truncation that helps the complexity of the calculation [37].

3.1.2 Python's Library *SCQubits*

SCQubits is an open-source Python library for simulating superconducting qubits. It provides tools for simulating and analyzing quantum circuits, with an emphasis on superconducting qubits.

The library includes functionalities for constructing Hamiltonians, simulating time evolution, computing spectra, and analyzing various aspects of superconducting qubit systems [38]. It is often used in the field of quantum computing and quantum information.

In this thesis, this library has been used for the simulations that required optimized calculations.

3.2 Experimental methods: resistance measurements

It is of key importance to control and calibrate the inductance of the coupling element that will be placed in the final chip so that we are sure that we will reach the USC regime. As we explained in Section 2.6, the resistivity of these inductors at normal temperature and their inductance are related. Henceforth, we will need to obtain these values experimentally with a four-probe station.

A four-probe station [39] is a device used to characterize the electrical properties of materials. It is a type of measurement setup that employs four individual probes to make contact with a sample or device under test. Two of the probes are used to inject a current into the sample, and the other two probes are used to measure the voltage.

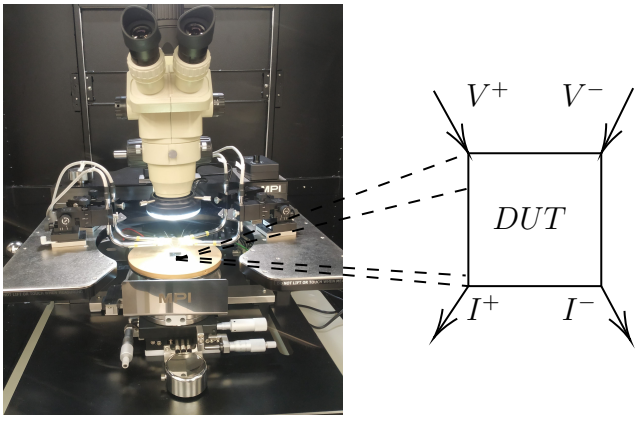

FIGURE 3.1: Laboratory set-up of a four-probe station at Quantum Computing Technologies Group IFAE and a scheme of the current and voltage probes applied to a Device Under Test (DUT).

This configuration, described in Figure 3.1, allows for precise and accurate measurements of resistivity, with key advantage being the eliminations of the effects of contact resistance. When only two probes are used (as in a two-point probe measurement), contact resistance can interfere with the accuracy of the measurements.

This methodology is used in this thesis to study a chip of thin Aluminum made at IFAE QCT group. In the following image, the station used in the experiments is shown, and the results obtained will be explained in Section 4.5.

Chapter 4

Results and Discussions

In this section of the thesis, results and their discussion are shown. Since we aim to study the coupling coefficient, the nature of the USC regime obligates us to study first the qubit and then the coupled system. Also, a brief experimental inside is shared on the estimated inductance of superconducting aluminium and its experimental limitations.

4.1 A simple circuit containing a Josephson Junctions: the RF-SQUID

We will provide the study of the simplest candidate that can be used for USC experiments with flux qubits: the RF-squid. We will show how to obtain the Hamiltonian, the eigenenergies and the main parameters involved in the system and its spectra.

4.1.1 Mathematical derivation of the Hamiltonian

To study the circuit, we will derive its Hamiltonian, using the equations and concepts introduced in Sections 2.1.1 and 2.2. From the circuit schematics depicted in Figure 4.1, one can derive the following set of relations between node and branch variables using equation (2.4),

$$\begin{cases} \phi_a = \phi_1 - \phi_0 \\ \phi_b = \phi_0 - \phi_1 + \phi_{ext} \end{cases} \tag{4.1}$$

where we have added to ϕ_{ext} the external flux because it is the closure branch. For each node, and in this case in node 1, the current conservation equation can be applied $I_L = I_{C_{sh}} + I_{C_J} + I_{JJ}$.

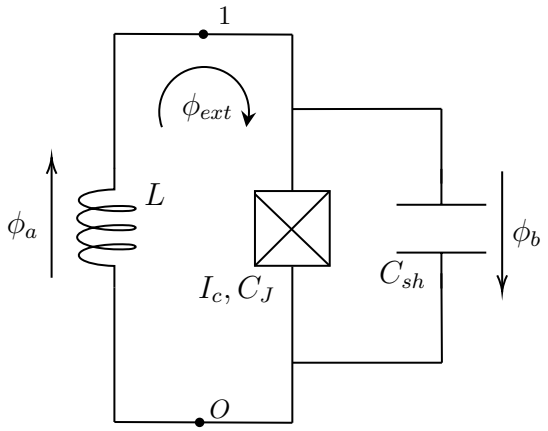

FIGURE 4.1: Circuit of an RF-squid with an external flux applied ϕ_{ext} clockwise, consisting of an inductor with inductance L, a Josephson junction with critical current I_c and capacitance C_J and a capacitance shunted C_{sh}. It also indicates the different nodes 1, O and the branch fluxes ϕ_a, ϕ_b.

Using equation (4.1), and defining $\phi_0 = 0$ as the ground and completing each intensity term

$$\underbrace{\frac{\phi_a}{L}}_{\text{IN}} = \underbrace{-(C_{sh}+C_J)\ddot{\phi}_a + I_c \sin\left(\frac{2\pi}{\Phi_0}(\phi_a - \phi_{ext})\right)}_{\text{OUT}}. \tag{4.2}$$

Integrating with respect to time, and considering (2.5), we obtain the following Lagrangian:

$$\mathcal{L} = \frac{C_{sh}+C_J}{2}\dot{\phi}_a^2 - \frac{1}{2L}\phi_a^2 + E_J \cos\left(\frac{2\pi}{\Phi_0}(\phi_a - \phi_{ext})\right). \tag{4.3}$$

We can perform the following change of variables to derive a simpler form of the Lagrangian

$$\begin{cases} \psi \equiv \frac{2\pi}{\Phi_0}\phi_a \\ f \equiv \frac{\phi_{ext}}{\Phi_0} \\ C_\Sigma = C_{sh} + C_J \end{cases} \Rightarrow \mathcal{L} = \left(\frac{\Phi_0}{2\pi}\right)^2 \frac{C_\Sigma}{2}\dot{\psi}^2 - \left(\frac{\Phi_0}{2\pi}\right)^2 \frac{1}{2L}\psi^2 + E_J \cos(\psi - 2\pi f). \tag{4.4}$$

Following the details described in equation (2.6), we proceed with the derivation of the Hamiltonian by calculating the conjugated momentum

$$p = \frac{\partial \mathcal{L}}{\partial \dot{\psi}} = \left(\frac{\Phi_0}{2\pi}\right)^2 C_\Sigma \dot{\psi}. \tag{4.5}$$

The last step consists of performing the Legendre transformation described in equation (2.7). With these changes, the Hamiltonian of the system is

$$\mathcal{H}_{RF} = p\dot{\psi} - \mathcal{L} = \left(\frac{\Phi_0}{2\pi}\right)^2 \frac{C_\Sigma}{2}\dot{\psi}^2 + \left(\frac{\Phi_0}{2\pi}\right)^2 \frac{1}{2L}\psi^2 - E_J \cos\left(\psi - 2\pi f\right). \tag{4.6}$$

Finally, introducing the canonical moment, and the definitions of E_c, β_L, and E_J, given in the Section 2.1.1 and promoting the flux and the charge operators, to quantum mechanical operators as we already showed in equation (2.8), the final Hamiltonian is obtained,

$$\hat{\mathcal{H}}_{RF} = \frac{4E_c}{\hbar^2}\hat{p}^2 + \frac{E_J}{2\beta_L}\hat{\psi}^2 - E_J \cos\Big(\hat{\psi} - 2\pi f\Big). \tag{4.7}$$

4.1.2 Study of the double well potential

The election of the parameters will determine whether the potential has a double well or not, a required condition to obtain a flux qubit. Using the condition that there are only 2 minima near the so-called sweet spot, we can find which parameter constraints must be respected for the RF-SQUID. Evaluating the potential at the sweet spot for convenience and calculating the derivative of the potential in equation (4.7) in respect to $\hat{\psi}$,

$$\hat{U}' = \frac{1}{E_J}\hat{U}(\hat{\psi}) = \frac{1}{2\beta_L}\hat{\psi}^2 + \cos\hat{\psi}. \tag{4.8}$$

Now, imposing the condition for a minimum in a single-variable system, we obtain a relation that

$$\frac{d\hat{U}'}{dt} = \frac{\hat{\psi}}{\beta_L} - \sin\hat{\psi} = 0 \Rightarrow \frac{\hat{\psi}}{\beta_L} = \sin\hat{\psi}. \tag{4.9}$$

Apart from the trivial solution $\psi = 0$, since β_L will determine the steepness of the first part of the equality, it is needed that $\beta_L > 1$ so that the two equations cross again. In Section 4.1.2, we show the design parameters chosen for the 1.5 GHz design[1],

- **Design RF-SQUID:** $I_c = 0.08\,\mu\text{A}$, $C = 43\,\text{fF}$, $L_c = 5.5\,\text{nH}$

which indeed fulfil $\beta_L > 1$, thus preserving a double well-potential.

[1]These parameters were chosen in other studies done by PhD student Alba Torras-Coloma.

4.1.3 Diagonalization and theoretical spectra

In this subsection, we aim to diagonalize the Hamiltonian and obtain its spectra with the numerical approach explained in Section 3.1.

4.1.3.1 Diagonalization

Once the RF-squid Hamiltonian in equation (4.6) is derived, we can transform its first two terms into a Harmonic oscillator (3.2) by defining $m = \frac{\hbar^2}{8E_c}$ and $\omega = \frac{2E_c}{\hbar}\sqrt{\frac{2E_J}{\beta_L E_c}}$, where m and ω would be the mass and frequency of the oscillator. We leave the third term of the Hamiltonian in equation (4.7) in terms of the phase representation, which is easy to solve numerically. In the case of the RF-SQUID's Hamiltonian, this procedure is key, since its second term, would be very difficult to represent on both basis. This fact will help us to obtain every matrix element in the harmonic eigenfunctions. Expressing $\hat{\mathcal{H}}$ with the ladder operators $\hat{a}$ and $\hat{a}^\dagger$,

$$\hat{\mathcal{H}} = \hbar\omega\hat{a}^\dagger\hat{a} - E_J \cos\left(\hat{\psi} - 2\pi f\right) \tag{4.10}$$

and giving now the trigonometric term in terms of the matrix elements

$$\mathcal{H}_{jk} = \hbar\omega\delta_{jk} - \frac{E_J}{2}\left(e^{-i2\pi f}\left\langle j\right| e^{i\hat{\psi}}\left|k\right\rangle + e^{i2\pi f}\left\langle j\right| e^{-i\hat{\psi}}\left|k\right\rangle\right). \tag{4.11}$$

The explicit expressions of the matrix elements $\langle j| e^{\pm i\phi} |k\rangle$ can be found in [40]. In Appendix A.1 we provide the Python code implementing the Hamiltonian diagonalization of the system.

4.1.3.2 Convergence of the candidate parameters and simulation

Before simulating the final spectra, the convergence of the solution will be assessed at $f = 0.5$. The idea of this step is to optimize as much as possible the number of bases required for the simulation.

As can be seen in Figure 4.2, the frequency transition quickly converges when increasing the number of bases used. A general tendency can be appreciated, since when increasing by 5 de basis number, the error descends 3 orders of magnitude. Our criteria to take a specific number of basis is based on the fact that lab equipment is precise up to Hz, so if the frequency transitions are of the order of GHz, we will require that the relative error is around $10^{-7} - 10^{-8}$. Henceforth, for the spectra simulations, depicted in Figure 4.2, $n_{trunc} = 18$ is used in the calculations since it suffices for the requirements.

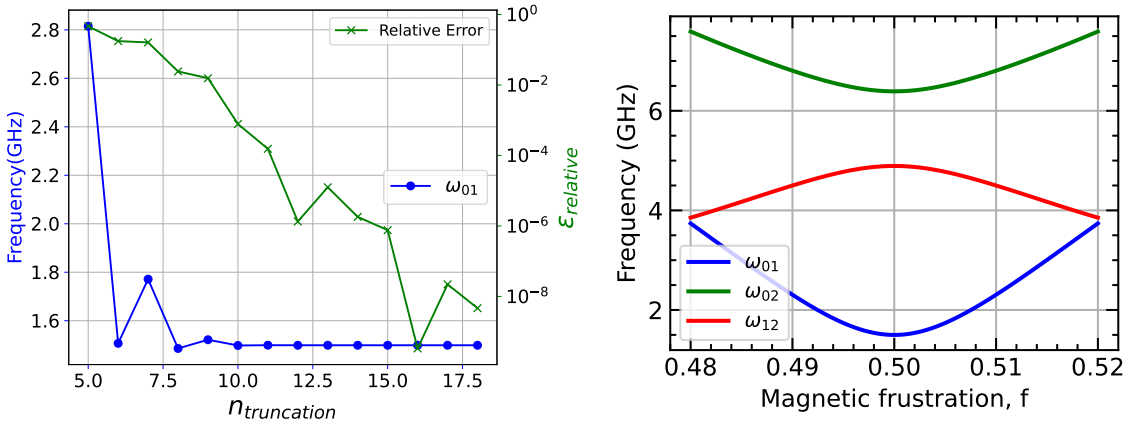

FIGURE 4.2: At the left is depicted the convergence of the frequency transition of the 1.5 GHz RF-SQUID for $f = 0.5$. In blue is depicted the ground-excited excitation frequency in GHz for each number of basis n_{trunc} used, and in green is depicted its relative error ($\epsilon_{relative}$). And at the right, the spectra of the 1.5 GHz RF-SQUID first three energy transitions for the parameters given in Section 4.1.2 and using $n_{trunc} = 18$ harmonic bases.

Even though, theoretically, the RF-SQUID can reach the USC when a resonator is added, practically it has some inconveniences. The main reason is the high dependence on the large inductance values, which can only be achieved with superinductor materials [41]. To obtain this inductance, it is important to calibrate precisely the evaporation of the granular aluminium, which can be a challenge. For instance, it is not easy to control parameters between evaporations. Even controlling precisely the sample parameters: pressure, oxygen flow, evaporation rate, etc. very different resistances can be obtained in the process (and thus inductance). Another inconvenience that may present is when the chip is baked, the properties of the material such as T_c and resistance can change [42].

4.2 Our candidate: C-shunted 3 Josephson junction flux qubit with non-negligible inductance.

In this section, the following C-shunted 3 Josephson junction flux qubit will be studied as a qubit candidate to reach the USC regime. The main difference with the RF squid is that the 3-JJ flux qubit contains 3 junctions instead of 1, providing better control over the parameters of the system. Furthermore, it requires smaller inductance values to reach the USC regime.

4.2.1 Mathematical derivation of the Hamiltonian

As in the derivation done in Section 4.1 for the RF-squid, to study the circuit, we start by giving the relation between node and branch flux variables following the schematics of Figure 4.3,

$$\begin{cases} \phi_1 = \phi_A - \phi_0 \\ \phi_2 = \phi_B - \phi_A \\ \phi_3 = \phi_C - \phi_B + \phi_{ext} \end{cases} \tag{4.12}$$

where we have used equation (2.4) and adding the external flux to ϕ_{ext} because it is a closure branch. Then, by imposing the current conservation and defining $\phi_0 = 0$

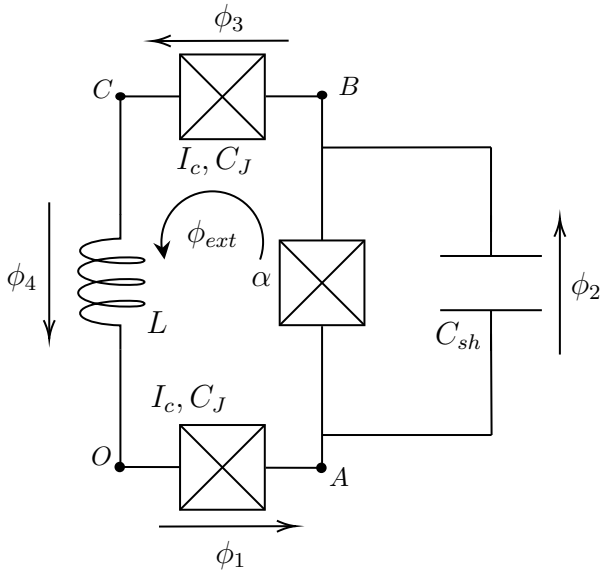

FIGURE 4.3: C-shunted 3 Josephson junction flux qubit scheme with an external fluxed applied ϕ_{ext} counter-clockwise. The circuit contains an inductor L, 3 Josephson junctions with two of them with critical current I_c and capacitance C_J with the third one αI_c, αC_J and a shunted capacitance C_{sh}. It also indicates the different nodes and the branch fluxes ϕ_1, ϕ_2 and ϕ_3.

as the ground, we can derive the equations of motion for each node.

- In node **A**

$$\begin{cases} \sum I_{in} = I_c \sin\left(\frac{2\pi}{\Phi_0}\phi_A\right) + C_J\ddot{\phi}_A \\ \sum I_{out} = \alpha I_c \sin\left(\frac{2\pi}{\Phi_0}(\phi_B - \phi_A)\right) + \bar{\alpha}C_J(\ddot{\phi}_B - \ddot{\phi}_A), \end{cases} \tag{4.13}$$

  where have also defined $\bar{\alpha} = \alpha + \frac{C_{sh}}{C_J}$ for convenience.

- In node **B**

$$\begin{cases} \sum I_{in} = \alpha I_c \sin\left(\frac{2\pi}{\Phi_0}(\phi_B - \phi_A)\right) + \bar{\alpha}C_J(\ddot{\phi}_B - \ddot{\phi}_A) \\ \sum I_{out} = \alpha I_c \sin\left(\frac{2\pi}{\Phi_0}(\phi_C - \phi_B)\right) + C_J(\ddot{\phi}_C - \ddot{\phi}_B), \end{cases} \tag{4.14}$$

- and in node **C**

$$\begin{cases} \sum I_{in} = I_c \sin\left(\frac{2\pi}{\Phi_0}(\phi_C - \phi_B)\right) + C_J(\ddot{\phi}_C - \ddot{\phi}_B) \\ \sum I_{out} = -\frac{\phi_C}{L}. \end{cases} \tag{4.15}$$

Now, integrating equations (4.13), (4.14), (4.15) with respect to time, and using the equation (2.5), leads to the following Lagrangian

$$\begin{aligned} \mathcal{L} \ = & \frac{C}{2}\dot{\phi}_A^2 + \bar{\alpha}\frac{C}{2}(\dot{\phi}_A - \dot{\phi}_B)^2 + \frac{C}{2}(\dot{\phi}_B - \dot{\phi}_C)^2 + E_J \cos\left(\frac{2\pi}{\Phi_0}\phi_A\right) \\ & + \alpha E_J \cos\left(\frac{2\pi}{\Phi_0}(\phi_B - \phi_A)\right) + E_J \cos\left(\frac{2\pi}{\Phi_0}(\phi_B - \phi_C)\right) - \frac{\phi_C^2}{2L}. \end{aligned} \tag{4.16}$$

Changing the variables from node fluxes to branch ones (4.12), the following Lagrangian is obtained

$$\begin{aligned} \mathcal{L} \ = & \frac{C}{2}\dot{\phi}_1^2 + \alpha\frac{C}{2}\dot{\phi}_2^2 + \frac{C}{2}\dot{\phi}_3^2 + E_J \cos\left(\frac{2\pi}{\Phi_0}\phi_1\right) + \alpha E_J \cos\left(\frac{2\pi}{\Phi_0}\phi_2\right) \\ & + E_J \cos\left(\frac{2\pi}{\Phi_0}\phi_3\right) - \frac{(\phi_1 + \phi_2 + \phi_3 - 2\pi f)^2}{2L}. \end{aligned} \tag{4.17}$$

Finally, we can do two last changes, firstly $\psi_i = (2\pi/\Phi_0)\phi_i$ and secondly, we can redefine the magnetic frustration $f \equiv \phi_{ext}/\Phi_0$, and using equations (2.6), (2.7) and adding the variable $\lambda = \phi_1 + \phi_2 + \phi_3 - 2\pi f$, we calculate the conjugated momentum

$$\frac{\partial \mathcal{L}}{\partial \dot{\psi}} = \begin{pmatrix} p_1 \\ p_2 \\ p_\lambda \end{pmatrix} = \Phi_0^2 C \begin{pmatrix} 1+\alpha & \alpha & -\alpha \\ \alpha & 1+\alpha & -\alpha \\ -\alpha & -\alpha & \alpha \end{pmatrix} \begin{pmatrix} \dot{\psi}_1 \\ \dot{\psi}_2 \\ \dot{\psi}_\lambda \end{pmatrix}. \tag{4.18}$$

Considering equation (2.7), we can perform a Legendre transformation to obtain the Hamiltonian of the 3JJ flux qubit system. The last step is to promote the flux and charge variables to quantum operators, as it was explained in equation (2.8). These changes yield the Hamiltonian of the C-sh 3JJ flux qubit with non-negligible loop inductance,

$$\hat{\mathcal{H}}_{3JJ+L} = \hat{T} + \hat{U},$$

$$\hat{T} = \frac{1}{2\Phi_0^2 C} \begin{pmatrix} \hat{p}_1 & \hat{p}_2 & \hat{p}_\lambda \end{pmatrix} \begin{pmatrix} 1 & 0 & 1 \\ 0 & 1 & 1 \\ 1 & 1 & \frac{1+2\bar{\alpha}}{\bar{\alpha}} \end{pmatrix} \begin{pmatrix} \hat{p}_1 \\ \hat{p}_2 \\ \hat{p}_\lambda \end{pmatrix}, \tag{4.19}$$

$$\hat{U} = E_J \left(\cos\hat{\psi}_1 + \cos\hat{\psi}_2 + \alpha \cos\left(\hat{\lambda} - \hat{\psi}_1 - \hat{\psi}_2 + 2\pi f\right) - \frac{1}{2\beta_L}\hat{\lambda}^2 \right).$$

4.2.2 Study of the double-well potential

Since we target a flux qubit, we have to study the potential to be sure that we can obtain a double-well. Evaluating the magnetic frustration at $f = 0.5$ and we normalize with respect to E_J, obtaining the following expression,

$$\hat{U}' = \frac{1}{E_J}\hat{U}(\hat{\psi}_1, \hat{\psi}_2, \hat{\lambda}) = -\cos\hat{\psi}_1 - \cos\hat{\psi}_2 + \alpha\cos\left(\hat{\lambda} - \hat{\psi}_1 - \hat{\psi}_2\right) + \frac{1}{2\beta_L}\hat{\lambda}^2. \tag{4.20}$$

Imposing the minima condition, we perform the gradient of the potential,

$$\nabla\hat{U}' = \begin{pmatrix} \sin\hat{\psi}_1 + \alpha\sin\left(\hat{\lambda} - \hat{\psi}_1 - \hat{\psi}_2\right) \\ \sin\hat{\psi}_2 + \alpha\sin\left(\hat{\lambda} - \hat{\psi}_1 - \hat{\psi}_2\right) \\ \frac{\hat{\lambda}}{\beta_L} - \alpha\sin\left(\hat{\lambda} - \hat{\psi}_1 - \hat{\psi}_2\right) \end{pmatrix} = \vec{0} \tag{4.21}$$

and if we subtract the first with the second equation, in the places where $\nabla\hat{U}' = 0$ we can redefine $\hat{\psi}_1 = \hat{\psi}_2 \equiv \hat{\psi}$. Also, adding up the second and the third equation in (4.21), $\hat{\lambda} = -\beta_L \sin\hat{\psi}$.

Considering these equalities, we shall define a one-variable-potential where all their points are either a maximum, a minimum or a turning point

$$\hat{U}'(\hat{\psi}) = -2\cos\hat{\psi} + \alpha\cos\left(\beta_L\sin\hat{\psi} + 2\hat{\psi}\right) + \frac{\beta_L}{2}\sin^2\hat{\psi}. \tag{4.22}$$

Nevertheless, because the potential was multivariable, the correct way would be to study the potential relative points with the Hessian matrix. The following method gives some constraints but, in the end, a numerical verification should be made since saddle points could be mistaken as minimum points.

Using the fact that the second-order term will indicate if we have a maximum or a minimum at the origin, and that the fourth-order term can create the double-well shape, the potential is expanded up to the fourth power with a Taylor series,

$$\begin{cases} \hat{U}'(\hat{\psi}) &= (\alpha-2) + A\hat{\psi}^2 + B\hat{\psi}^4 + \mathcal{O}(\hat{\psi}^6) \\ A &= 1 + \frac{\beta_L}{2} - \frac{\alpha}{2}(2+\beta_L)^2 < 0 \\ B &= \frac{1}{12}(2\alpha\beta_L(2+\beta_L) - 1) > 0 \end{cases} \Rightarrow \alpha > \frac{1}{2+\beta}. \tag{4.23}$$

The third order does not appear because of our election of magnetic frustration, which gives rise to a symmetric potential, simplifying our work. Using the parameters of the designed chip,

- **Design 3JJ+L:** $C_J = 5.0\,\text{fF}$, $I_c = 0.2\,\mu\text{A}$, $\alpha = 0.55$, $C_{sh} = 25\,\text{fF}$, $L_c = 0.4\,\text{nH}$

it can be depicted that, even counting on some flaws in fabrications[2], the double well would remain, as seen in Figure 4.4. We must emphasize the advantages of

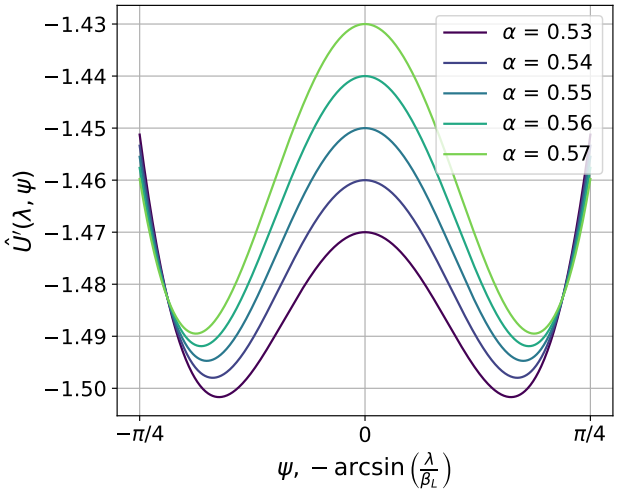

FIGURE 4.4: Cut of the potential 4.20 between the two minima for the used parameters 4.2.2 of the qubit and varying α emulating flaws of fabrication in sizes of the junctions.

these qubits in front of the RF-SQUID, since we only need inductances of an order of magnitude less.

[2]These fabrication flaws can come from errors within sizes, asymmetries, deviation from the critical current and stray capacitance among others.

4.2.3 Diagonalization and spectra

In this chapter, we aim to diagonalize the Hamiltonian and obtain its spectra with the numerical approach explained in Section 3.1.2. In this case, we utilize *SCQubits* because the 3JJ qubit is numerically more complex than RF-SQUID, and it requires optimization. In the Appendix A.2 we provide the Python code implementing the Hamiltonian diagonalization of the system with *SCQubits*. In this study of the convergence for $f = 0.5$, we will demand convergence up to the order of Hz of the spectral calculation. This condition will assure us that the eigenfunctions used give

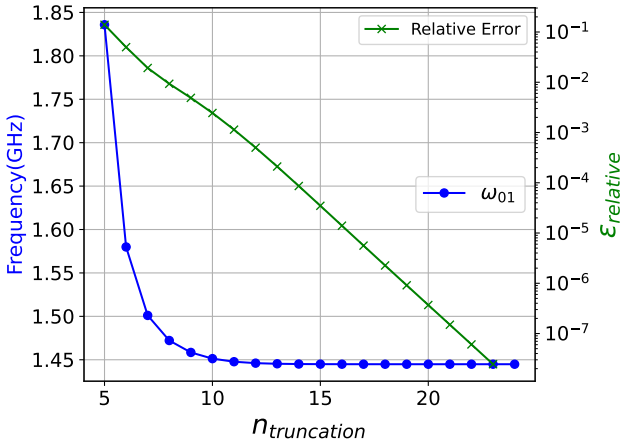

FIGURE 4.5: Convergence of the frequency transition of the 1.5 GHz three junction flux qubit for $f = 0.5$. In blue is depicted the ground-excited excitation frequency in GHz for each number of basis used, and in green is depicted its relative error ($\epsilon_{relative}$).

a precise coupling calculation. Following this criteria, and considering Figure 4.5, we can see that using a 21 harmonic basis for each degree of freedom will suffice.

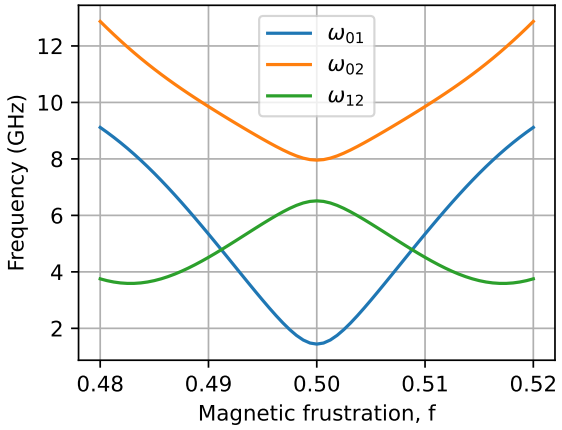

FIGURE 4.6: Spectra of the 1.5 GHz three junction flux qubit for the parameters given in 4.2.2 using $n_{trunc} = 21$ harmonic bases.

4.3 The coupled system: C-shunted 3 Josephson junction flux qubit coupled to an LC resonator

In this section of the thesis, we provide the study of our target system, the C-shunted Josephson junction qubit with a galvanically coupled resonator. We will show the Hamiltonian derivation, its spectra and the calculations of the coupling coefficient, which we expect to be on the USC regime.

4.3.1 Mathematical derivation of the Hamiltonian

The purpose of this section is to obtain the full system Hamiltonian and match each term with (2.11). If we can obtain a pure interaction term, we will be able to calculate numerically the expected coupling term.

First and foremost, we start by representing schematically the full system, which is the same as in Section 4.2, but with a resonator galvanically attached.

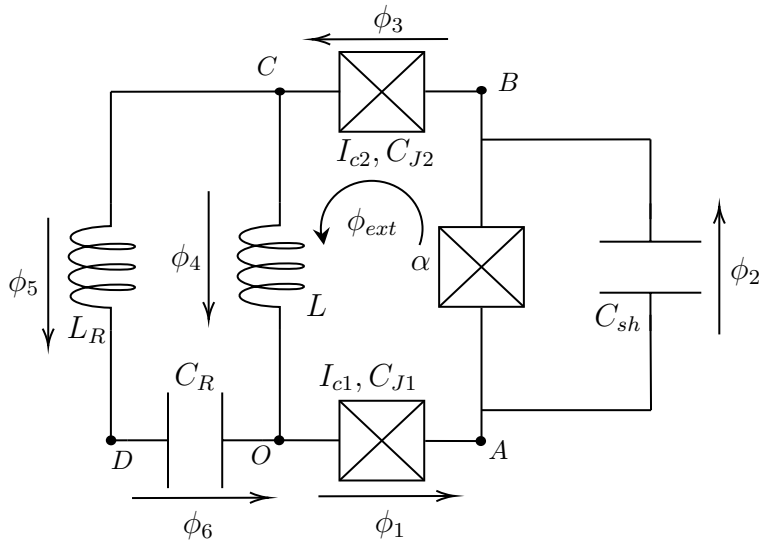

FIGURE 4.7: C-shunted 3 Josephson junction flux qubit coupled to an LC resonator by a shared inductance, with an external fluxed applied ϕ_{ext} counterclockwise. The circuit contains an inductor L, 3 Josephson junctions with two of them with critical current I_c and capacitance C_J with the third one αI_c, αC_J and a shunted capacitance C_{sh}. It is coupled to a resonator within an inductor L_R and a capacitance, C_R It also indicates the nodes and the branch fluxes ϕ_i.

To study the circuit, we start by defining $\phi_0 = 0$ as the ground of the system and apply Kirchoff's law in each node. For node **A**

$$C_J\ddot{\phi}_A + (\alpha C_J + C_{sh})(\ddot{\phi}_A - \ddot{\phi}_B) = -I_0 \sin\left(\frac{2\pi}{\Phi_0}\phi_A\right) - \alpha I_0 \sin\left(\frac{2\pi}{\Phi_0}(\phi_A - \phi_B)\right). \quad (4.24)$$

For node **B**

$$\begin{aligned}(\alpha C_J + C_{sh})(\ddot{\phi}_B - \ddot{\phi}_A) + (\lambda_2 + \beta_2)C_J(\ddot{\phi}_B - \ddot{\phi}_C) = \\ - \alpha I_0 \sin\left(\frac{2\pi}{\Phi_0}(\phi_B - \phi_A)\right) - \beta_2 I_0 \sin\left(\frac{2\pi}{\Phi_0}(\phi_B - \phi_C)\right).\end{aligned} \tag{4.25}$$

For the node **C**

$$C_J(\ddot{\phi}_D - \ddot{\phi}_B) = I_0 \sin\left(\frac{2\pi}{\Phi_0}(\phi_C - \phi_B)\right) - \frac{1}{L_C}\phi_C - \frac{1}{L_R}(\phi_C - \phi_D). \tag{4.26}$$

And finally, for node **D**

$$C_R\ddot{\phi}_D = -\frac{1}{L_R}(\phi_D - \phi_C). \tag{4.27}$$

Integrating over time the equations of motion (4.24), (4.25), (4.26) and (4.27), and by using the Euler-Lagrange equation (2.5) we obtain the Lagrangian of the system

$$\begin{aligned}\mathcal{L} =& \frac{C_J}{2}\dot{\phi}_A^2 + \frac{\alpha C_J + C_{sh}}{2}(\dot{\phi}_A - \dot{\phi}_B)^2 + \frac{C_J}{2}(\dot{\phi}_B - \dot{\phi}_C)^2 + \\ &+ \frac{C_R}{2}\dot{\phi}_D^2 + E_J \cos\left(\frac{2\pi}{\Phi_0}\phi_A\right) + E_J \cos\left(\frac{2\pi}{\Phi_0}(\phi_C - \phi_B\right) + \\ &+ \alpha E_J \cos\left(\frac{2\pi}{\Phi_0}(\phi_B - \phi_A)\right) - \frac{1}{2L_c}\phi_C^2 - \frac{1}{2L_R}(\phi_C - \phi_D)^2.\end{aligned} \tag{4.28}$$

Then, changing node to branch flux variables following the defined directions in Figure 4.7, where we defined ϕ_4 as the closure branch. To give an easier form of the Lagrangian and remove the flux-dependent variable, we define $\phi_6 \equiv \phi_R$, use phase variables $\varphi_i = (2\pi/\Phi_0)\phi_i$, and transform the magnetic frustration $f \equiv \phi_{ext}/\Phi_0$. Taking into account the flux branches, $\phi_2 = \phi_{ext} - \phi_1 - \phi_3 - \phi_4$. All these transformations bring us

$$\begin{aligned}\mathcal{L} = &\left(\frac{\Phi_0}{2\pi}\right)^2 \left(\frac{C_J}{2}\dot{\varphi}_1^2 + \frac{\alpha C_J + C_{sh}}{2}(\dot{\varphi}_1 + \dot{\varphi}_3 + \dot{\varphi}_4)^2 + \frac{C_J}{2}\dot{\varphi}_3^2 + \frac{C_R}{2}\dot{\varphi_R}^2\right) + \\ &+ E_J \cos\varphi_1 + E_J \cos\varphi_3 + \alpha E_J \cos(\varphi_1 + \varphi_3 + \varphi_4 - f) - \\ &- \left(\frac{\Phi_0}{2\pi}\right)^2 \left(\frac{1}{2L_c}\varphi_4^2 + \frac{1}{2L_R}(\varphi_4 - \varphi_R)^2\right).\end{aligned} \tag{4.29}$$

As the final steps, we must calculate the generalized momentum, where we have also defined $\bar{\alpha} = \alpha C_J + C_{sh}$ for convenience

$$\frac{\partial \mathcal{L}}{\partial \dot{\varphi}} = \begin{pmatrix} p_1 \\ p_3 \\ p_4 \\ p_R \end{pmatrix} = \bar{\alpha}\left(\frac{\Phi_0}{2\pi}\right)^2 \begin{pmatrix} 1 + \frac{C_J}{\bar{\alpha}} & 1 & 1 & 0 \\ 1 & 1 & 1 & 0 \\ 1 & 1 & 1 & 0 \\ 0 & 0 & 0 & \frac{C_R}{\bar{\alpha}} \end{pmatrix} \begin{pmatrix} \dot{\varphi}_1 \\ \dot{\varphi}_3 \\ \dot{\varphi}_4 \\ \dot{\varphi}_R \end{pmatrix} \tag{4.30}$$

to perform the Legendre transformation. And remembering to promote flux and charge into quantum operators, this transformation will yield us a Hamiltonian which consists of three parts, each part contains the following terms

$$\hat{\mathcal{H}}_{qubit} = \left(\frac{2\pi}{\Phi_0}\right)^2 \left\{ \frac{(\hat{p}_1 - \hat{p}_4)^2}{2C_J} + \frac{(\hat{p}_3 - \hat{p}_4)^2}{2C_J} + \frac{\hat{p}_4^2}{2\bar{\alpha}} + \left(\frac{1}{2L_c} + \frac{1}{2L_R}\right)\hat{\varphi}_4^2 \right\} - \\ - E_J \cos\hat{\varphi}_1 - E_J \cos\hat{\varphi}_3 - E_J \cos\left(\hat{\varphi}_1 + \hat{\varphi}_3 + \hat{\varphi}_4 - 2\pi f\right) \tag{4.31}$$

$$\hat{\mathcal{H}}_{res} = \left(\frac{2\pi}{\Phi_0}\right)^2 \frac{\hat{p}_R^2}{2C_R} + \left(\frac{\Phi_0}{2\pi}\right)^2 \frac{1}{2L_R}\hat{\varphi}_R^2 \tag{4.32}$$

$$\hat{\mathcal{H}}_{int} = -\frac{E_J}{\beta_{L,R}}\hat{\varphi}_4\hat{\varphi}_R. \tag{4.33}$$

4.3.2 Diagonalization and spectra

Once we get the Hamiltonian of the full system, we can simulate its spectra. For the same reasons as in Section 4.2.3, we will use *SCQubits*.

Studying the USC regime of this system does not require precise eigenenergies and eigenvalues of the full system. So, in this case, we only aim to depict an approximate form of the spectra.

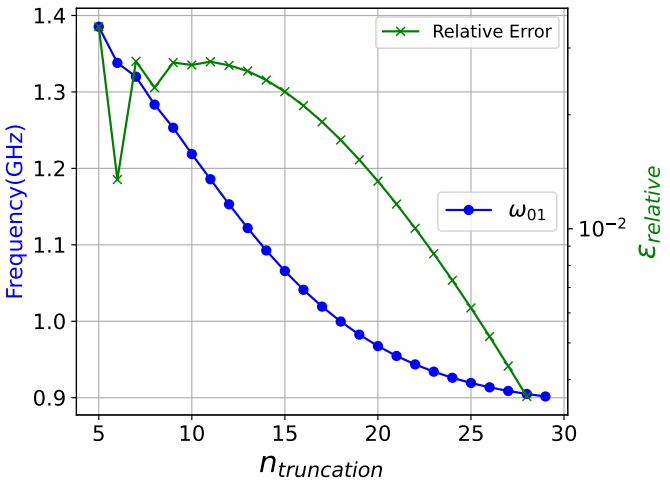

FIGURE 4.8: Convergence of the frequency transition of the 1.5 GHz three junction flux qubit coupled to a resonator for $f = 0.5$. In blue is depicted the ground-excited excitation frequency in GHz for each number of basis used, and in green is depicted its relative error ($\epsilon_{relative}$).

Even though in Figure 4.8 we can appreciate that the spectra have not converged with the criteria of Hz precision, we will not target more precise calculations, since the dimensions of the system are computationally challenging for a regular computer.

In Appendix A.3 we provide the Python code implementing the Hamiltonian diagonalization of the system that is depicted in Figure 4.9. In the context of this

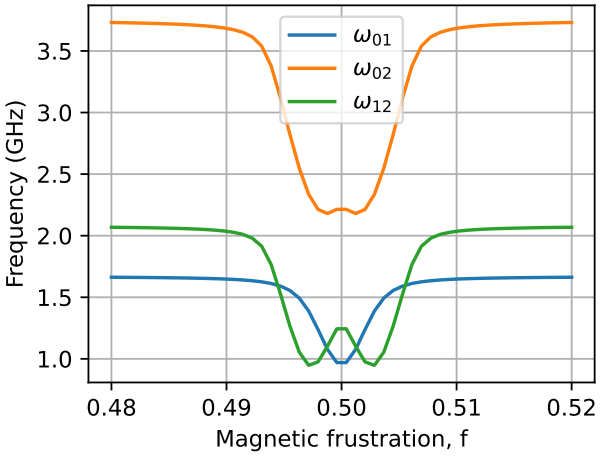

FIGURE 4.9: Spectra of the 1.5 GHz three junction flux qubit with a 1.5 GHz coupled resonator for the parameters given in 4.2.2 and 4.3.2 using $n_{trunc} = 21$ harmonic bases.

thesis, the parameters of the LC resonator are:

- **Design 1.5 GHz resonator:** $C_r = 3.46 \cdot 10^3$ fF, $L_r = 2.95$ nH.

These are chosen so that the frequency of resonance coincides with the qubit to have maximum coupling.

4.4 Study of the coupling coefficient

Once the interaction Hamiltonian is obtained, we can study the coupling coefficient of the full system. This coefficient g, will indicate if we have achieved the USC regime. To obtain it, we will follow the methodology described in the supplementary material of [43] and [44]. This approximated method requires expressing the interacting Hamiltonian based on the qubit and the phase of the resonator $\hat{\varphi}_R$ in terms of annihilation/creation operators

$$\hat{\mathcal{H}}_{int} = -\frac{E_J}{\beta_{L,R}}\hat{\varphi}_4\hat{\varphi}_R = -\frac{E_J}{\beta_{L,R}}\sqrt{\frac{\hbar}{2m_R\omega_R}}(\hat{a}^\dagger + \hat{a}) \sum_{k,k'=0,1} \langle k|\,\hat{\varphi}_4\,|k'\rangle\,|k'\rangle\,\langle k|\,. \tag{4.34}$$

Now, rewriting the operator for convenience

$$\hat{\mathcal{H}}_{int} = \sum_{\alpha=x,y,z} \hbar g_\alpha(\hat{a}^\dagger + \hat{a})\hat{\sigma}_\alpha = \hbar \underbrace{\begin{pmatrix} g_z & g_x e^{-i\xi} \\ g_x e^{i\xi} & -g_z \end{pmatrix}}_{g} (\hat{a}^\dagger + \hat{a}) \tag{4.35}$$

where we have defined g_α as the coupling coefficient, we have used the Pauli matrices $\{\hat{\sigma}_x, \hat{\sigma}_y, \hat{\sigma}_z\}$ and ξ is a phase. Calculating the absolute value of the determinant of this 2×2 coupling matrix, we obtain that, with the parameters used for the system, the coupling coefficient is $\frac{g}{\omega_r} \approx 0.458$.

This parameter fulfils the USC regime criteria, $0.1 < g/\omega_r < 1$. Therefore, we conclude that the system can achieve the USC regime. Furthermore, we must emphasize the importance of the coupling inductance. Figure 4.10 shows the rapid increase of the coupling when increasing L_c.

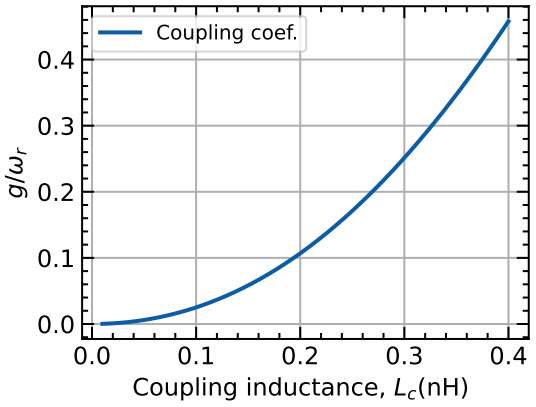

FIGURE 4.10: Coupling coefficient simulation on the dependence on the coupling inductance L_c.

In Appendix A.4 we provide the Python code that calculates the coupling coefficient for this system.

4.5 Characterization of the chip: first steps

In this experimental section of the thesis, we depict some measurements and insides of the first steps of characterizing a chip at IFAE QCT. This section does not enclose all the processes and information required for the fabrication of an SQC, since it is a complex and advanced matter done by IFAE QCT group's researchers. Instead, a part in the characterization of the inductance of aluminum is explained in the following chip[3].

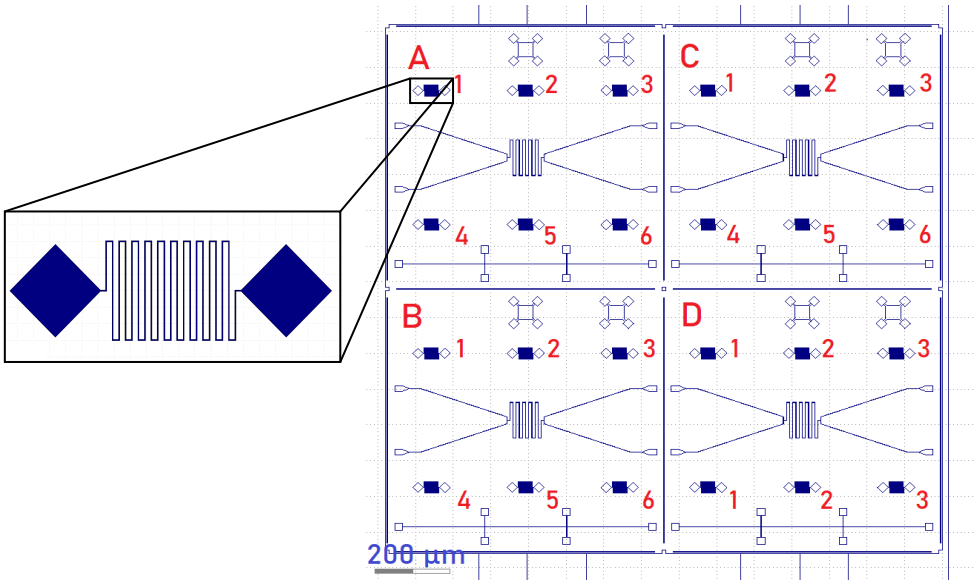

FIGURE 4.11: Aluminum (in blue) chip design studied with a dimension of 7.400 mm x 7.400 mm and 20 mm of thickness, with indications of identification of each structure. Also, a zoom of the A1 structure is shown of size 200 μm x 100 μm.

To estimate the inductance of the structure, we have measured its structure's resistance with a four-probe station, with the procedure explained in Section 3.2. Even though it is required to do the measurements at 4K, we did them at room temperature since we did not have access to the refrigerator to do the measurements. Nonetheless, this is valid to estimate the inductance of the system. Proceeding with the measurements and sending an array of intensities and voltages, a lineal fit is done using Appendix B.1 to obtain each resistance, obtaining the following experimental results.

[3]made by Alba Torras-Coloma in December 2023

	A1	A2	A5	A6	B1	B2	B5	B6	D4
$R_{\square}$ ($\Omega/\square$)	3.9357	4.5585	4.3660	4.8562	4.3215	4.2542	4.2909	4.4140	5.0448
$u_{R_{\square}}$ ($m\Omega/\square$)	5.7	6.7	5.5	14.9	7.2	7.0	5.8	9.5	13
$L_{kin\square}$ ($pH/\square$)	4.6052	5.3339	5.1087	5.6823	5.0567	4.9779	5.0209	5.1649	5.9029
$u_{L_{kin\square}}$ ($fH/\square$)	6.7	7.8	6.4	17.5	8.4	8.1	6.7	11.1	15.6

TABLE 4.1: Square resistance $R_{\square}$, its uncertainty $u_{R_{\square}}$, the kinetic inductance $L_{kin\square}$ and its uncertainty $u_{L_{kin\square}}$ of every structure that has not suffered damage from fabrication and conservation. The number of squares per structure is 1483.

Even though all the structures were intended to be equal, the experimental results show the difficulty of controlling the parameters of thin film fabrication. Nonetheless, using the fact that all structures are equal, we can calculate an average value for the resistance of a square $\bar{R}_{\square} = 4.45 \pm 0.11\ \Omega/\square$ and using equation (2.13) to estimate the kinetic inductance, we obtain that the 20 nm Al has an approximate sheet kinetic inductance of $\bar{L}_{kin,\square} = 5.21 \pm 0.13$ pH/$\square$.

This result indicates that our designed parameters can be achieved needing only 77 squares. In the case of the targeted design, we have a space of 30 μm for the inductance. Since we can produce wires with a width of 75 nm at least, we will be able to obtain the desired inductance with only $\sim$6 μm, which is lower than required. Moreover, the statistical deviation of approximately 2.5% depicts the reproducibility of the method and the USC regime will be achieved even with a small variation of the coupling inductance, as it was demonstrated in Figure 4.10. This results demonstrate that Al wires can be used in order to obtain large inductances and therefore help us reach the USC regime.

Chapter 5

Conclusions

In this thesis, we have introduced the main concepts behind the technology of superconducting quantum circuits. In particular, we have been familiarized with circuit quantization theory. Moreover, we have presented flux qubits galvanically coupled to a resonator, as a promising device to achieve the ultrastrong coupling regime of light-matter interaction.

Intending to study the USC regime, we have derived the Hamiltonians of the main flux qubits and the coupled 3JJ-LC system. In particular, we have calculated the eigenenergies and eigenvectors using different numerical methods. These have proven the computational difficulties within the USC regime.

Moreover, we have provided a calculation of the coupling coefficient of our design circuit, proving the ability to achieve the ultrastrong coupling regime.

Finally, we have characterized a chip with thin Al wires. Proving that although aluminum is not a superinductor material, it would be viable to be used to couple a flux qubit and a resonator and achieving USC.

Appendix A

Codes

A.1 Code for solving the spectra of an RF-SQUID

```
PI = np.pi
SUP_FLUX_QUANTUM = 2.067833831e-15 #SI
E = 1.6021766208e-19 # C
Ic = (2*0.04)*1e-6 #mA
C = (41+50*0.04)*1e-15 #fF
L = 5.5e-9 #nH
Ec = E*E/(2*C)
beta = 2*PI*Ic*L/SUP_FLUX_QUANTUM
f0 = 0.5
f = np.linspace(0.49,0.51,100)
h_barra = 1.054571817e-34
m = h_barra**2/(8*Ec)
Ej = Ic * SUP_FLUX_QUANTUM / (2*PI)
omega = 2*Ec/h_barra*np.sqrt(2*Ej/(beta*Ec))
theta = np.sqrt(h_barra/(m*omega))
max = 30

def abs_e_iphi(l ,k ):
  min_kl = np.minimum(k, l)
  k_fac = np.math.factorial(k)
  l_fac = np.math.factorial(l)
  prefactor = np.exp(-theta**2/4)/(np.sqrt(2.0**(k+l)*k_fac*l_fac))
  eiphi = 0.
  for i in range(min_kl+1):
    eiphi += 2**i*np.math.factorial(i)*math.comb(k,i)*math.comb(l,i
   )*(-1)**i*theta**(l+k-2*i)*1j**(l+k)
  return prefactor*eiphi

def abs_e_menysiphi(l ,k ):
  abs_e_menysiphi = abs_e_iphi(l ,k )*(-1)**(l+k)
  return abs_e_menysiphi

def Hlk(l,k,fru):
```

```
33   if l==k:
34     H_lk = (k)*h_barra*omega - 0.5*Ej*(np.cos(2*PI*fru)*(abs_e_iphi
     (l,k)+abs_e_menysiphi(l,k))+ 1j*np.sin(2*PI*fru)*(abs_e_iphi(l,k
     )-abs_e_menysiphi(l,k)))
35
36   else:
37     H_lk =  - 0.5*Ej*(np.cos(2*PI*fru)*(abs_e_iphi(l,k)+
     abs_e_menysiphi(l,k))+ 1j*np.sin(2*PI*fru)*(abs_e_iphi(l,k)-
     abs_e_menysiphi(l,k)))
38
39   return  H_lk
40
41 import matplotlib.pyplot as plt
42 from scipy.optimize import curve_fit
43
44 #Calculations
45 Eground = []
46 Eexcited = []
47 Eexcited2 = []
48 Edif = []
49 EdifJ=[]
50 Edif2 = []
51
52 Hamiltonian = np.zeros((max,max), dtype=complex)
53
54 #Hamiltonian construction and diagonalization:
55 for fru in f:
56   for l in range(max):
57     for k in range(max):
58       Hamiltonian.put(max*l+k, Hlk(l,k,fru))
59   Etot_vals, Etot_vects =  np.linalg.eigh(Hamiltonian)
60   Eground.append(convert_J_to_GHz(np.sort(Etot_vals)[0]))
61   Eexcited.append(convert_J_to_GHz(np.sort(Etot_vals)[1]))
62   Eexcited2.append(convert_J_to_GHz(np.sort(Etot_vals)[2]))
63   Edif.append(convert_J_to_GHz(np.sort(Etot_vals)[1]-np.sort(
      Etot_vals)[0]))
64   EdifJ.append(np.sort(Etot_vals)[1]-np.sort(Etot_vals)[0])
65   Edif2.append(convert_J_to_GHz(np.sort(Etot_vals)[2]-np.sort(
      Etot_vals)[0]))
```

A.2 Three-junction flux qubit with non-negligible inductance spectra solver

```
E = 1.6021766208e-19 #SI
Flux0 = 2.067833831e-15 #SI
Ic = convert_uA_to_A(2*0.1)
C = convert_fF_to_F(50*0.1)
Csh = convert_fF_to_F(25)
Ec = convert_J_to_GHz(E*E/(2*C))
Ecsh = convert_J_to_GHz(E*E/(2*Csh))
Ej = convert_J_to_GHz(Ic*Flux0/(2*np.pi))
L = convert_nH_to_H(0.4)
El = convert_J_to_GHz(Flux0**2/(4*L*np.pi**2))
alpha = 0.55
flux_list= np.linspace(0.48, 0.52, 100)
drei_jj_Csh = """branches:
- [JJ,1,4,{},{}]
- [JJ,4,2,{},{}]
- [JJ,3,2,{},{}]
- [L,1,3,{}]
- [C,4,2,{}]""".format(Ej,Ec,Ej*alpha,Ec/alpha,Ej,Ec,El,Ecsh)
drei_JJ_qubit = scq.Circuit(drei_jj_Csh, from_file=False, ext_basis
    = 'harmonic')
drei_JJ_qubit.sym_hamiltonian()
drei_JJ_qubit.var_categories
drei_JJ_qubit.external_fluxes
drei_JJ_qubit.cutoff_names
drei_JJ_qubit.cutoff_ext_3 = 18
drei_JJ_qubit.plot_evals_vs_paramvals("$\phi$ 1", flux_list,
    evals_count=3, subtract_ground=True)
```

A.3 Three-junction flux qubit with non-negligible inductance coupled to a resonator spectra solver

```
# Set qubit parameters
alpha = 0.55
Jc    = 2.0   # uA/um^2
area  = 0.1   # um^2
Csh   = 25.04    # fF
Sc    = 50    # fF/um^2
Cc    = 1.01   # fF
# Set LC resonator parameters
Lr = 2.95   # nH
Cr = 3.46e3   # fF

# Set coupling
Lc = 0.4   # nH
EJ = calculate_Ej(Jc, area)
Ec = calculate_Ec(Sc * area)
Ec_alph = calculate_Ec(Sc * area * alpha + Csh)

# Now convert the coupling capacitance to Ec in GHz
Ec_cc = calculate_Ec(Cc)
# Inductive coupling energy
ELc = calculate_El(Lc)

# Resonator energies
ELres = calculate_El(Lr)
Ecres = calculate_Ec(Cr)
# define the circuit
flux_res_circuit = """branches:
- [JJ,0,1,{},{}]
- [JJ,1,2,{},{}]
- [JJ,2,3,{},{}]
- [L,3,0,{}]
- ["L", 3, 4, {}]
- ["C", 4, 0, {}]
""".format(EJ, Ec,
           EJ, Ec,
           alpha * EJ, Ec_alph,
           ELc,
           ELres,
           Ecres)

fluxres = scq.Circuit(flux_res_circuit, from_file=False,
                              ext_basis="harmonic")
fluxres.external_fluxes
fluxres.hamiltonian_symbolic
# Set the cutoff values - check names
fluxres.cutoff_names
fluxres.cutoff_n_1 = 7
fluxres.cutoff_n_2 = 7
fluxres.cutoff_ext_3 = 18
```

```
50 fluxres.cutoff_ext_4 = 18
51 fluxvals = np.linspace(0.48, 0.52, 35)
52 spectrum = fluxres.get_spectrum_vs_paramvals(" 1 ", fluxvals,
       evals_count=3,
53                                             subtract_ground=True,
       get_eigenstates=True);
```

A.4 Code g calculation

```
"""
Calculates the coupling coefficient of the circuit:
    3JJ qubit inductively coupled (by sharing an inductance) to a
   resonator

Author: Alba Torras-Coloma
@ QCT
"""
def build_hamilt_without_Vi(n_max_charge, n_max, alpha, gamma, EC,
   EJ, beta_L):
    """Builds all hamiltonian terms that do not contain f"""

    # Matrix sizes for charge and ho basis
    N_tot = 2 * n_max_charge + 1
    N_ho = n_max + 1

    # Consider Csh
    a_fact = alpha + gamma

    # Charge identity matrices
    idty_charge = sparse.identity(N_tot, format='csr')
    # Harmonic oscillator identity
    idty_ho = sparse.identity(N_ho, format='csr')

    # Build Tf matrix
    Nsqrt_matrix = build_Nsqrt_charge_matrix(N_tot, n_max_charge)
    Tf = (EC / 2) *build_Tf_matrix_3JJ(Nsqrt_matrix, idty_charge,
                                            idty_ho, a_fact)

    # Build Ti matrix
    N_charge_matrix = build_N_charge_matrix(N_tot, n_max_charge)
    a_plus_adagger = build_ho_a_adagger_matrix(N_ho)

    sum_inverse_alpha = (1 + 2 * a_fact)/a_fact
    prefactor_p_matrix = (EJ / (4 * beta_L * EC)) /
   sum_inverse_alpha

    ho_p_matrix = a_plus_adagger * 1j * (prefactor_p_matrix ** (1 /
    4))

    Ti = - EC * build_Ti_matrix_3JJ(N_charge_matrix, idty_charge,
                                        ho_p_matrix, a_fact)

    # Build TV matrix
    N_ho_matrix = build_N_ho_matrix(N_ho)
    prefactor_TV = np.sqrt(EC * EJ * sum_inverse_alpha / beta_L)
    TV = build_TV_matrix_3JJ(idty_charge, N_ho_matrix) *
   prefactor_TV

    # Build Vf matrices
    exp_iphi_matrix = build_exp_i_phi_matrix(N_tot)
```

```
47      prefactor_Vf = - EJ / 2
48      Vf = prefactor_Vf * build_Vf_matrix_3JJ(exp_iphi_matrix,
49                                                  idty_charge,
    idty_ho)
50
51      return Tf + Ti + TV + Vf
52
53  def build_Vi_without_f(n_max_charge, n_max, Ec, beta,
54                         a_fact):
55      N_ho = n_max + 1
56      N_tot = 2 * n_max_charge + 1
57
58      # Build Vi matrices (inside loop for f)
59      EP = build_EP_matrix_3JJ(N_ho, Ec, Ec, beta,
60                                       a_fact)
61      exp_iphi_matrix = build_exp_i_phi_matrix(N_tot)
62      Vi_1st_part = build_1st_Vi_without_2pif_3JJ(exp_iphi_matrix, EP
    )
63
64      return Vi_1st_part
65
66  def diagonalize_hamiltonian(Hamiltonian, en_levels):
67      """
68      Diagonalizes the Hamiltonian and returns the states,
    eigenenergies and
69      the spectrum
70      Args:
71          Hamiltonian: hamiltonian of the system
72          en_levels: number of energy levels to be calculated.
73
74      Returns:
75
76      """
77      energies, states = linalg.eigsh(Hamiltonian, k=en_levels, which
    ='SA',
78          return_eigenvectors=True)
79      states = np.matrix.transpose(states)
80      states = [x for y, x in sorted(zip(energies, states))]
81
82      energies = np.sort(energies)
83      energies = np.array(energies)   # States reordered in previous
    line
84      states = np.array(states)
85
86      spectrum = []
87      for i in range(1, en_levels):
88          spectrum.append(energies[i] - energies[0])
89
90      spectrum = np.asarray(spectrum)
91
92      return energies, spectrum, states
93
94  def expected_value(matrix, state_left, state_right):
```

```
    """
    Expected value phi_L (in h.o. basis), recall phi_L =
    (a + a_dagger)*prefactor

    state_left - row vector
    state_right - column vector
    """

    left_times_matrix = np.dot(state_left, matrix)
    exp_val = np.dot(left_times_matrix, state_right)

    return exp_val

def build_phi_lamb_matrix(Ec, Ej, alpha, beta, n_max, n_max_charge):
    """
    Builds the complete phi matrix needed to obtain the coupling
    coefficient
    Args:
        Ec: charging energy
        Ej: current energy
        alpha: ratio small-reference junction
        beta: ratio inductances
        a_matrix: annihilation operator

    Returns:
    """
    size_ho = n_max + 1
    size_charge = 2 * n_max_charge + 1

    charge_idty = sparse.identity(size_charge, format='csr')
    alpha_fact = (2*alpha + 1) / alpha
    #prefactor = ((2*Ec/Ej) * alpha_fact * beta) ** (1/4)
    prefactor = (beta * Ec * alpha_fact / (4 * Ej)) ** (1/4)
    a_adagger_matrix = build_ho_a_plus_adagger_matrix(size_ho)

    phi_matrix = sparse.kron(sparse.kron(charge_idty, charge_idty),
        a_adagger_matrix) * prefactor

    return phi_matrix.toarray()




n_max = 20  # Max N for harmonic oscillator states
n_max_charge = 10  # Max N for Cooper pair states
en_levels = 6  # Maximum number of energy levels computed


# Define the main variables of the system
Lc = 0.37    # nH
Lr = 3.24     # nH
alpha = 0.53
```

```
146 area = 0.065    # um^2
147 Jc = 3.0    # uA/um^2
148 Sc = 70     # fF/um^2
149 Csh = 50    # fF
150
151 CJ = Sc * area
152
153 gamma = Csh / CJ    # This will go with alpha (capacitive terms)
154 a_fact = alpha + gamma
155
156 Ec = calculate_Ec(CJ) * 8
157 Ej = calculate_Ej(Jc, area)
158 beta_Lc = calculate_beta_L(Lc, Jc, area)
159 beta_Lr = calculate_beta_L(Lr, Jc, area)
160
161 sum_inv_beta = (1/beta_Lr) + (1/beta_Lc)
162
163 f = 0.5
164 # Maybe calculating it at 0.5 is enough
165 # f_range = np.linspace(0.49, 0.51, 10)
166
167 # Build the Hamiltonian with all terms
168 Hamilt_without_vi = build_hamilt_without_Vi(n_max_charge, n_max,
    alpha,
169                                             gamma, Ec, Ej, 1/
    sum_inv_beta)
170
171 Vi_prefactor = - alpha * Ej / 2
172 Vi_1st_part = build_Vi_without_f(n_max_charge, n_max, Ec, 1/
    sum_inv_beta,
173                  a_fact)
174
175 Vi = Vi_prefactor * (np.exp(1j * 2 * np.pi * f) * Vi_1st_part +
176                      np.exp(-1j * 2 * np.pi * f) * Vi_1st_part.
    conj().T)
177
178 Hamiltonian = Hamilt_without_vi + Vi
179
180 # Diagonalize the inductance + qubit system
181 energies, spectrum, states = diagonalize_hamiltonian(Hamiltonian,
    en_levels)
182
183 #print(states[0])
184 #print(spectrum[0])
185 #print(np.dot(states[0], states[1].conj().T))
186
187 # Compute gx, gz
188 # Build the operator matrix
189 phi_matrix = build_phi_lamb_matrix(Ec, Ej, a_fact, 1/sum_inv_beta,
    n_max,
190                                    n_max_charge)
191 dim = 6
192 overlaps = np.zeros((dim,dim), dtype=np.complex_)
```

```
193 for i in range(dim):
194     for j in range(dim):
195         overlaps[i, j] = expected_value(phi_matrix, states[i],
196                                         states[j].conj().T)
197 print(overlaps)
198
199 alpha_fact = (2 * a_fact + 1) / a_fact
200 prefactor_g = (Ej / (2 * beta_Lr)) * ((2 * Ec / Ej) * alpha_fact *
201                                       beta_Lr) ** (1 / 4)
202 g = prefactor_g*np.absolute(np.linalg.det(np.array([[overlaps[0,0],
    overlaps[0,1]],[overlaps[1,0],overlaps[1,1]]])
203 print("g = ", g)
```

Appendix B

Experimental results treatment

B.1 Linear fit of the measurements

```
import numpy as np
from sklearn.linear_model import LinearRegression

# Example data (replace this with your own data)
current = np.array(I_list)
voltage = np.array(v_list)

# Reshape the data if needed
current = current.reshape(-1, 1)
voltage = voltage.reshape(-1, 1)

# Create and fit the linear regression model
model = LinearRegression()
model.fit(current, voltage)

# Extract the slope (resistance) and intercept from the model
resistance = model.coef_[0][0]
intercept = model.intercept_[0]

# Calculate the uncertainty in the slope (resistance)
coefficients, cov_matrix = np.polyfit(current.flatten(), voltage.
    flatten(), 1, cov=True)
resistance_uncertainty = np.sqrt(np.diag(cov_matrix))[0]

# Print the estimated resistance and intercept along with
    uncertainty
print(f"Estimated Resistance (R): {resistance} ohms    {
    resistance_uncertainty} ohms")
print(f"Intercept: {intercept}")

# Make predictions using the model
predicted_voltage = model.predict(current)

```

```
#Plot the results
import matplotlib.pyplot as plt

plt.scatter(current, voltage, label='Actual Data')
plt.plot(current, predicted_voltage, color='red', label='Linear
    Regression')
plt.xlabel('Current (A)')
plt.ylabel('Voltage (V)')
plt.legend()
plt.show()
```

References

[1] A. Cho, Science **365**, 1364 (2019).

[2] M. Steffen, D. P. DiVincenzo, J. M. Chow, T. N. Theis, and M. B. Ketchen, IBM Journal of Research and Development **55**, 13 (2011).

[3] F. Arute, K. Arya, R. Babbush, D. Bacon, J. C. Bardin, R. Barends, R. Biswas, S. Boixo, F. G. Brandao, D. A. Buell, et al., Nature **574**, 505 (2019).

[4] Q.-C. Sun, Y.-L. Mao, S.-J. Chen, W. Zhang, Y.-F. Jiang, Y.-B. Zhang, W.-J. Zhang, S. Miki, T. Yamashita, H. Terai, et al., Nature Photonics **10**, 671 (2016).

[5] R. Barends, L. Lamata, J. Kelly, L. García-Álvarez, A. G. Fowler, A. Megrant, E. Jeffrey, T. C. White, D. Sank, J. Y. Mutus, et al., Nature communications **6**, 7654 (2015).

[6] T. Niemczyk, F. Deppe, H. Huebl, E. Menzel, F. Hocke, M. Schwarz, J. Garcia-Ripoll, D. Zueco, T. Hümmer, E. Solano, et al., Nature Physics **6**, 772 (2010).

[7] G. Wendin, Reports on Progress in Physics **80**, 106001 (2017).

[8] S. Danilin and M. Weides, *Quantum sensing with superconducting circuits* (2021), 2103.11022.

[9] P. Adhikari, M. Hafezi, and J. M. Taylor, Phys. Rev. Lett. **110**, 060503 (2013).

[10] A. Blais, S. M. Girvin, and W. D. Oliver, Nature Physics **16**, 247 (2020).

[11] F.-M. Liu, M.-C. Chen, C. Wang, S.-W. Li, Z.-X. Shang, C. Ying, J.-W. Wang, C.-Z. Peng, X. Zhu, C.-Y. Lu, et al., *Quantum design for advanced qubits: plasmonium* (2022), 2109.00994.

[12] A. Frisk Kockum, A. Miranowicz, S. De Liberato, S. Savasta, and F. Nori, Nature Reviews Physics **1**, 19 (2019).

[13] D. López-Núñez, Ph.D. thesis, Programa de Doctorat en Física, Universitat de Barcelona (2023).

[14] M. H. Devoret, *Quantum fluctuations (les houches session lxiii)* (1997).

[15] P. Forn-Díaz, L. Lamata, E. Rico, J. Kono, and E. Solano, Reviews of Modern Physics **91**, 025005 (2019).

[16] J. J. García Ripoll, *Quantum Information and Quantum Optics with Superconducting Circuits* (Cambridge University Press, 2022).

[17] D. Pozar, *Microwave Engineering, 4th Edition* (Wiley, 2011), ISBN 9781118213636, URL https://books.google.es/books?id=JegbAAAAQBAJ.

[18] A. Mizel, *Theory of superconducting qubits beyond the lumped element approximation* (2023), 2211.10852.

[19] P. Krantz, M. Kjaergaard, F. Yan, T. P. Orlando, S. Gustavsson, and W. D. Oliver, Applied physics reviews **6** (2019).

[20] A. A. Golubov, M. Y. Kupriyanov, and E. Il'Ichev, Reviews of modern physics **76**, 411 (2004).

[21] P. Forn-Díaz, Ph.D. thesis, Delft University of Technology (2010).

[22] I. M. Pop, K. Geerlings, G. Catelani, R. J. Schoelkopf, L. I. Glazman, and M. H. Devoret, Nature **508**, 369 (2014).

[23] J. J. García-Ripoll and B. Peropadre, *Lecture notes on superconducting quantum circuits* (2014), URL https://juanjose.garciaripoll.com/lectures-quantum-circuits/index.html.

[24] M. H. Devoret and R. J. Schoelkopf, Science **339**, 1169 (2013).

[25] A. Parra-Rodriguez, *Canonical quantization of superconducting circuits* (2021), 2104.09410.

[26] W. Smith, A. Kou, U. Vool, I. Pop, L. Frunzio, R. Schoelkopf, and M. Devoret, Physical Review B **94**, 144507 (2016).

[27] R. Harris, J. Johansson, A. Berkley, M. Johnson, T. Lanting, S. Han, P. Bunyk, E. Ladizinsky, T. Oh, I. Perminov, et al., Physical Review B **81**, 134510 (2010).

[28] T. L. Robertson, B. L. T. Plourde, P. A. Reichardt, T. Hime, C.-E. Wu, and J. Clarke, Phys. Rev. B **73**, 174526 (2006), URL https://link.aps.org/doi/10.1103/PhysRevB.73.174526.

[29] I. I. Rabi, Phys. Rev. **51**, 652 (1937).

[30] J. Dupont-Roc and G. e. a. Grynberg, Basic Process and Appilcations (1992).

[31] F. Valenti, F. Henriques, G. Catelani, N. Maleeva, L. Grünhaupt, U. von Lüpke, S. T. Skacel, P. Winkel, A. Bilmes, A. V. Ustinov, et al., Physical review applied **11**, 054087 (2019).

[32] D. López-Núñez, Q. P. Montserrat, G. Rius, E. Bertoldo, A. Torras-Coloma, M. Martínez, and P. Forn-Díaz (2023).

[33] A. Torras-Coloma, L. M. de Olcoz, E. Céspedes, E. Bertoldo, D. López-Núñez, S. Paul, W. Wernsdorfer, G. Rius, and P. Forn-Díaz (2023).

[34] P. Aumann, T. Menke, W. D. Oliver, and W. Lechner, New Journal of Physics **24**, 093012 (2022).

[35] P. Groszkowski and J. Koch, Quantum **5**, 583 (2021).

[36] M. Abramowitz and I. A. Stegun, *Handbook of Mathematical Functions with Formulas, Graphs, and Mathematical Tables* (Dover Publications, New York, 1972), ISBN 0-486-61272-4.

[37] S. M. Girvin, *Circuit QED: Superconducting Qubits Coupled to Microwave Photons* (Oxford University Press, 2011).

[38] S. Pavan Chitta, T. Zhao, Z. Huang, I. Mondragon-Shem, and J. Koch, arXiv e-prints pp. arXiv–2206 (2022).

[39] G. Panta and D. Subedi, Kathmandu University journal of science, Engineering and technology **8**, 31 (2012).

[40] W. Witschel, European Journal of Physics **17**, 357 (1996).

[41] M. Bell, I. Sadovskyy, L. Ioffe, A. Y. Kitaev, and M. Gershenson, Physical review letters **109**, 137003 (2012).

[42] J. Bourassa, J. M. Gambetta, A. A. Abdumalikov Jr, O. Astafiev, Y. Nakamura, and A. Blais, Physical Review A **80**, 032109 (2009).

[43] A. Tomonaga, H. Mukai, F. Yoshihara, and J.-S. Tsai, Physical Review B **104**, 224509 (2021).

[44] B. Peropadre, D. Zueco, D. Porras, and J. J. García-Ripoll, Phys. Rev. Lett. **111**, 243602 (2013).